

Enhancement of Wigner crystallization in quasi low-dimensional solids.

G. Rastelli¹, P. Quémerais², and S. Fratini²

¹ *Istituto Nazionale di Fisica della Materia and Dipartimento di Fisica Università dell'Aquila, via Vetoio, I-67010 Coppito-L'Aquila, Italy and*

² *Laboratoire d'Etudes des Propriétés Electroniques des Solides, CNRS BP 166 - 25, Avenue des Martyrs, F-38042 Grenoble Cedex 9, France*

(Dated: January 25, 2006)

The crystallization of electrons in quasi low-dimensional solids is studied in a model which retains the full three-dimensional nature of the Coulomb interactions. We show that restricting the electron motion to layers (or chains) gives rise to a rich sequence of structural transitions upon varying the particle density. In addition, the concurrence of low-dimensional electron motion and isotropic Coulomb interactions leads to a sizeable stabilization of the Wigner crystal, which could be one of the mechanisms at the origin of the charge ordered phases frequently observed in such compounds.

I. INTRODUCTION

Despite being a well established concept in the physics of interacting electrons, direct evidence of Wigner crystallization¹ has been reported unambiguously in only a limited number of systems, namely electrons at the surface of liquid helium,^{2,3,4} and in semiconductor heterostructures of extreme purity.⁵ In both cases, a two dimensional electron gas (2DEG) is realized at an interface between two media, for which the jellium model of the homogeneous electron gas constitutes a good approximation.

Alternatively, the charge ordering phenomena observed at low temperatures in a number of *solids* have been either interpreted as some form of Wigner crystallization, or ascribed to the presence of long-ranged Coulomb interactions. These include the one-dimensional organic salts TTF-TCNQ,⁶ (TMTTF)₂X,^{7,8} (DI-DCNQI)₂Ag,⁹ the ladder cuprate compounds Sr₁₄Cu₂₄O₄₁^{10,11} and chain compounds Na_{1+x}CuO₂,¹² as well as the layered superconducting cuprates^{14,15} and possibly the two-dimensional BEDT-TTF organic salts.¹³ For such systems, the jellium model is *a priori* a rather crude modelization, and the concept of Wigner crystallization must be generalized to account for other competing effects such as the periodic potential of the underlying lattice, chemical impurities, structural defects, magnetic interactions, etc. In narrow band solids, for instance, the interplay with the host lattice of ions can strongly affect the charge ordering pattern especially at highly commensurate band fillings.^{6,16} Nevertheless, when the radius of localization of the particles is larger than the typical ion-ion distance, the host lattice can be replaced to a good accuracy by an effective continuous medium, restoring *de facto* the validity of the jellium model.^{17,18}

Setting aside the important problem of the commensurability with the host lattice, and neglecting disorder and other effects that can certainly play a role in the compounds under study, we come to the following observation: a common feature shared by the experimental systems listed above is that they are all *quasi low-dimensional* solids, i.e. they are bulk three-dimensional (3D) compounds where the transfer integrals between dif-

ferent chemical units are so anisotropic that the carrier motion is effectively restricted to two-dimensional (2D) atomic layers, or one-dimensional (1D) chains. Yet, the Coulomb forces retain their three-dimensional character, being long-ranged and *isotropic*. In such systems, interlayer (inter-chain) interactions cannot be neglected, leading eventually to a full three-dimensional ordering of the charges.^{11,15} This suggests why quasi low-dimensional solids are a particularly favorable ground for the observation of Wigner crystallization: the electron-electron interactions have the same behavior as in bulk three-dimensional systems, but the kinetic part is strongly reduced by the effective lowering of dimensionality. Reminding that a Wigner crystal arises from the competition between potential and kinetic energy, this results in a sizeable stabilization of the crystal as compared with the usual 3D case.⁴²

A similar conclusion is reached by observing that, even compared to purely low-dimensional systems such as the 2DEG mentioned above, the Wigner crystal phase could be stabilized in quasi low-dimensional solids due to the presence of additional interlayer interactions. This topic has been analyzed in the literature in the framework of bilayer quantum wells, i.e. constituted of two coupled 2D electron systems, where it has been shown that, depending on the strength of the interlayer forces, the ordering pattern can differ from the hexagonal structure expected in a single layer.^{19,20} More importantly, it was found^{21,22,23} that at interlayer separations comparable with the mean interparticle distance, the melting density is raised by a factor of 3 with respect to the pure 2D case, which makes a factor as large as 10² when appropriately scaled to the 3D situation.

In this work, we model quasi two-dimensional (one-dimensional) systems as periodic arrays of conducting layers (wires) embedded in a three-dimensional bulk material, where the electrons interact through isotropic long-range Coulomb forces. We show that, upon varying the particle density or the interlayer (interwire) separation, the Wigner crystal undergoes several structural transitions in order to minimize its energy compatibly with the given geometrical constraints. We then give a semi-quantitative estimate of the melting density for the

different structures previously identified, based on the Lindemann criterion, which confirms the stabilization of the crystallized phase expected from general grounds.

The paper is organized as follows: In Section II, we introduce a model for the crystallization of electrons in an anisotropic environment and the method for calculating the crystal energy in the harmonic approximation, which includes the classical Madelung energy and the zero-point vibrational energy of the collective excitations. This is applied to the case of quasi two-dimensional systems, for which the structural/melting phase diagram is determined. The validity of the present approximation scheme is checked at the end of Section II by analyzing a system of two coupled layers, for which our results compare positively with the numerical results available in the literature. An analogous discussion for quasi one-dimensional systems is reported in Section III, by treating explicitly the case where the conducting chains form a square array. The main results are summarized in section IV.

II. WIGNER CRYSTALLIZATION IN LAYERED SOLIDS

A. Model and approximations

Let us consider a system of electrons (or holes) of density $n = (4\pi r_s^3/3)^{-1}$ in a strongly anisotropic environment, such that the particle motion is constrained to equally spaced atomic layers (at distance d), but remains isotropic within the layers. To ensure charge neutrality, we assume a uniform 3D compensating background of opposite charge. The hamiltonian for N crystallized particles in a volume V is given by:

$$H = NE_M + \sum_{i=1}^N \frac{p_i^2}{2m} + V_d \quad (1)$$

The first term

$$E_M = \frac{e^2}{2} \left[\sum_i \frac{1}{R_i} - n \int_V \frac{d\vec{r}}{r} \right] \quad (2)$$

is the Madelung energy of the given lattice structure (in the thermodynamic limit, $N, V \rightarrow \infty$, boundary effects are negligible and all particles become equivalent). The second term is the *two-dimensional* kinetic energy of the localized particles and the last term accounts for the interactions due to the *planar* displacements $\vec{u}_i = (u_{xi}, u_{yi})$ of the electrons around their equilibrium positions:

$$V_d = \frac{e^2}{2} \sum_{i \neq j} \left[\frac{1}{|\vec{R}_i + \vec{u}_i - \vec{R}_j - \vec{u}_j|} - \frac{1}{|\vec{R}_i - \vec{R}_j|} \right] \quad (3)$$

Expanding the last term for small displacements results in a series expansion for the energy Eq. (1) in

powers of $1/r_s^{1/2}$.^{24,25} The leading term, proportional to $1/r_s$, corresponds to the Madelung energy E_M of Eq.(2). In free space, it attains its minimum value $E_{BCC} = -0.89593/r_s$ (in atomic units) for a Body Centered Cubic (BCC) Wigner crystal.²⁶ The second term in the expansion, proportional to $1/r_s^{3/2}$, is the zero point energy of the particle fluctuations in the harmonic approximation, which also depends on the selected crystal structure. It is negligible for $r_s \rightarrow \infty$, and remains smaller than the Madelung term by typically an order of magnitude at $r_s \sim 100$. Nonetheless, it can play an important role in determining the relative stability of the different crystal structures, especially when approaching the melting density. Higher orders in the energy expansion^{24,25} include anharmonic ($1/r_s^p$ with $p \geq 2$) and exchange terms of the form $e^{-c\sqrt{r_s}}$, which we shall neglect in the following discussion.

Up to quadratic order in the displacements, our model Hamiltonian reads:

$$H = NE_M + \sum_i \frac{p_i^2}{2m} + \frac{e^2}{4} \sum_{i,j \neq i} (\vec{u}_i - \vec{u}_j) \hat{I}_{ij} (\vec{u}_i - \vec{u}_j) \quad (4)$$

where \hat{I}_{ij} is a 2×2 matrix characterizing the dipole-dipole interactions, given by $(\alpha, \beta = x, y)$:

$$\left(\hat{I}_{ij} \right)_{\alpha\beta} = \frac{3\vec{R}_{ij,\alpha}\vec{R}_{ij,\beta}}{|\vec{R}_{ij}|^5} - \frac{\delta_{\alpha\beta}}{|\vec{R}_{ij}|^3} \quad (5)$$

with $\vec{R}_{ij} = \vec{R}_i - \vec{R}_j$. The most general elementary Bravais lattice compatible with a given layered structure is identified by a couple of basis vectors describing the ordering within the planes, $\vec{A}_1 = (a_1, 0, 0)$, $\vec{A}_2 = (a_{2x}, a_{2y}, 0)$, and a third vector $\vec{A}_3 = (a_{3x}, a_{3y}, d)$ which sets the relative shift (a_{3x}, a_{3y}) between two equivalent 2D-lattices on neighboring planes. Other structures, with more than one particle per unit cell, are possible in principle, but will not be considered here.

Due to the additional lengthscale d introduced by the layered constraint, the crystal energy is no longer a function of r_s alone. Its dependence on the lattice geometry is best expressed by introducing a dimensionless parameter γ , which measures of the relative importance of interlayer and intralayer interactions. It is defined as the ratio between the mean interparticle distance in the planes and the interlayer separation, namely $\gamma = \sqrt{\pi} r_{s,2D}/d$. Here $r_{s,2D}$ defines the 2D density parameter in the individual layers, related to the bulk r_s by $r_{s,2D}^2 = 4r_s^3/3d$. The first two terms of the low-density expansion, corresponding respectively to the Madelung energy and the zero-point fluctuation energy in the quadratic model (4) can be written in compact form as:

$$E = \frac{A(\gamma)}{r_s} + \frac{B(\gamma)}{r_s^{3/2}}. \quad (6)$$

It should be noted that an effective mass $m^* \neq m$ and a dielectric constant $\kappa \neq 1$ can be straightforwardly included in the model through a redefinition of the Bohr

radius $a_B \rightarrow a_B^* = a_B \kappa (m/m^*)$, unit energy $me^4/\hbar^2 \rightarrow m^*e^4/\kappa^2\hbar^2$, and density parameter $r_s \rightarrow r_s(m^*/m)/\kappa$. Hereafter, energies and lengths will therefore be expressed in terms of these effective units, characterizing the host medium. A much more complex situation arises in systems with a frequency-dependent dielectric screening, leading to the formation of polarons, for which the reader is referred to Refs.^{15,27}.

B. Minimization of the Madelung energy

Following the hierarchy of the series expansion introduced above, we start by searching for the layered configuration which minimizes the electrostatic repulsion between the particles, which is appropriate in the limit of large r_s . The calculation is performed by standard Ewald summation techniques, which split the slowly convergent series in Eq. (2) into two exponentially converging sums.²⁸ Given the interlayer separation d and the bulk density n (or, alternatively, given the pair of dimensionless parameters γ and r_s) we are left with 4 free minimization parameters: 2 for the inplane structure, 2 for the interlayer ordering.

The result of the minimization for the Madelung coefficient A in the range $0 < \gamma < 6$ is illustrated in Fig. 1. Two distinct regimes can be identified. In the limit of large separations ($\gamma \lesssim 1$), the coupling between the layers is weak, and the resulting planar pattern is hexagonal, with a staggered interlayer ordering, i.e. the particles on the neighboring layers falling on top of the centers of the triangles. The sharp rise of the Madelung constant in this regime is due to the fact that the compensating background is distributed homogeneously in three-dimensional space, which penalizes strongly anisotropic charge distributions.⁴³

Upon reducing the interlayer separation so that $\gamma \gtrsim 1$, the increasing interlayer interactions make the hexagonal pattern energetically unfavorable. Above $\gamma = 1.15$, a more isotropic ordering of the charges is stabilized, which presents a centered rectangular (CR) structure in the planes. Further increasing γ leads to a sequence of structures whose planar patterns are respectively squared (S, in the interval $1.32 < \gamma < 2.13$), rectangular (R, $2.13 < \gamma < 2.84$), centered rectangular (CR, $2.86 < \gamma < 4.31$), a generic rhombic, or oblique phase (Rh, $4.31 < \gamma < 4.45$), then hexagonal again, and so on. Such phases are all connected by continuous structural transitions, with the exception of the hexagonal structure, which is attained through a discontinuous change of the crystal parameters. Note that in the very narrow interval $2.84 < \gamma < 2.86$, a generic structure with rhombic planar symmetry is stabilized, which allows to evolve continuously from the rectangular to the centered rectangular patterns (not shown). The sequence of structural transitions goes on at larger values of γ .

The interlayer ordering is shown at the bottom of Fig.1. It is staggered for the first three patterns (H), (CR) and

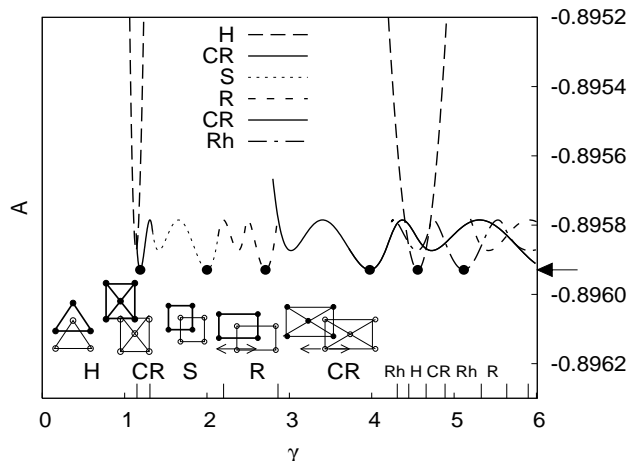


FIG. 1: Madelung coefficient A in atomic units for different crystal structures constrained to a layered environment, as a function of the anisotropy ratio γ . The different curves correspond to different planar configurations: hexagonal (H), square (S), centered rectangular (CR), rectangular (R) and rhombic (Rh). The interlayer orderings in the simplest cases at low γ are sketched below the curves (for the R and CR structures, the stacking varies as indicated by the double arrows). The resulting three-dimensional Wigner crystal reduces to a perfect BCC at the points marked by filled dots, whose energy is indicated by the horizontal arrow.

(S) for $\gamma \lesssim 2$, as expected for large interlayer separations, where the relative ordering is fully determined by the coupling between two adjacent planes, and indeed coincides with what is found in bilayer systems¹⁹ (see Section IIE below). At larger values of γ , the interactions beyond the nearest planes become relevant, which makes the simple staggered ordering unfavorable. For instance, a staggered/non-staggered transition takes place within the rectangular phase at $\gamma = 2.46$, corresponding to a relative sliding of the planar structures on adjacent planes in the direction of the long bonds (indicated by the double arrow in Fig. 1).

Remarkably, each of the phases identified above contains a special point γ^* where the ideal BCC structure — which has the lowest possible Madelung energy in three dimensions — is itself compatible with the layered constraint. The different planar configurations identified above then correspond to the different ways of cutting a BCC by an array of equally spaced layers. Such points are easily calculated by setting the distance $d = 2\pi/|\mathbf{K}|$, with \mathbf{K} any reciprocal lattice vector, and correspond to $\gamma^* = 2^{1/4}$, 2, $2^{1/4}3^{3/4}$, $2^{1/4}5^{3/4}$, $2 \cdot 3^{3/4}$, etc... Similarly, the higher relative minima visible in Fig. 1 correspond to different orientations of the same three-dimensional Face Centered Cubic (FCC) ordering.

Away from such special points, the overall charge distribution remains very isotropic in all the region $\gamma \gtrsim 1$, as testified by the extremely small deviations of the Madelung energy from the ideal case, $\Delta E_M \lesssim 10^{-4}/r_s$. Such small energy variations, however, refer to the op-

timal structures obtained at different values of γ , which *does not mean* that the electrostatic repulsion between the carriers is irrelevant in the determination of the charge ordering patterns in real systems: in a given compound, where both the interlayer distance and the density are fixed, one should rather compare the energies of two competing phases at *fixed* γ . For example, enforcing a hexagonal symmetry at $\gamma = 2$, where the optimal structure is squared, would cost an energy $\Delta E_M \sim 0.015/r_s \sim 200K$ at $r_s = 20$, which is comparable with the typical charge ordering energy scales in solids. Yet, since the Madelung energy is determined by the interactions with a large number of (distant) neighbors, the structures found here are expected to be relatively soft against local deformations. The situation is different regarding global symmetry changes, as can result from the inclusion of a periodic potential of competing symmetry, which could strongly modify the sequence and order of the structural transitions, possibly favoring the appearance of alternative phases.^{29,30}

C. Zero point fluctuation energy

The next term in the series expansion of the ground state energy Eq. (6) corresponds to the quantum zero point fluctuations of the particles around their equilibrium positions, in the harmonic approximation. It is negligible at large r_s (low density), but it becomes quantitatively important at lower r_s , where it can slightly modify the sequence of phases identified in the preceding Section. Upon further reducing r_s , this term eventually drives the quantum melting of the crystal, that will be analyzed in the next Section.

The calculation of the fluctuation term proceeds as follows. The harmonic model Eq.(4) is diagonalized by introducing the normal modes $q_{s,\vec{k}}$

$$\vec{u}_i = \frac{1}{\sqrt{N}} \sum_{s,\vec{k}} \hat{\varepsilon}_{s,\vec{k}} e^{i\vec{k}\cdot\vec{R}_i} q_{s,\vec{k}} \quad (7)$$

where $\hat{\varepsilon}_{s,\vec{k}}$ are the two-dimensional polarization vectors (the electrons oscillate within the planes) and the vector \vec{k} runs through the Brillouin zone of the *three-dimensional* reciprocal lattice. This yields two branches $s = 1, 2$ of collective modes with eigenfrequencies $\omega_{s,\vec{k}}$, so that the vibrational energy per particle can be expressed as:

$$E_V = \frac{1}{N} \sum_{s,\vec{k}} \frac{\hbar\omega_{s,\vec{k}}}{2} \quad (8)$$

It is useful to introduce the normalized density of states (DOS) of the collective modes, that we write here in general as:

$$\rho(\omega) = \frac{1}{DN} \sum_{s=1}^D \sum_{\vec{k} \in BZ} \delta(\omega - \omega_{s,\vec{k}}) \quad (9)$$

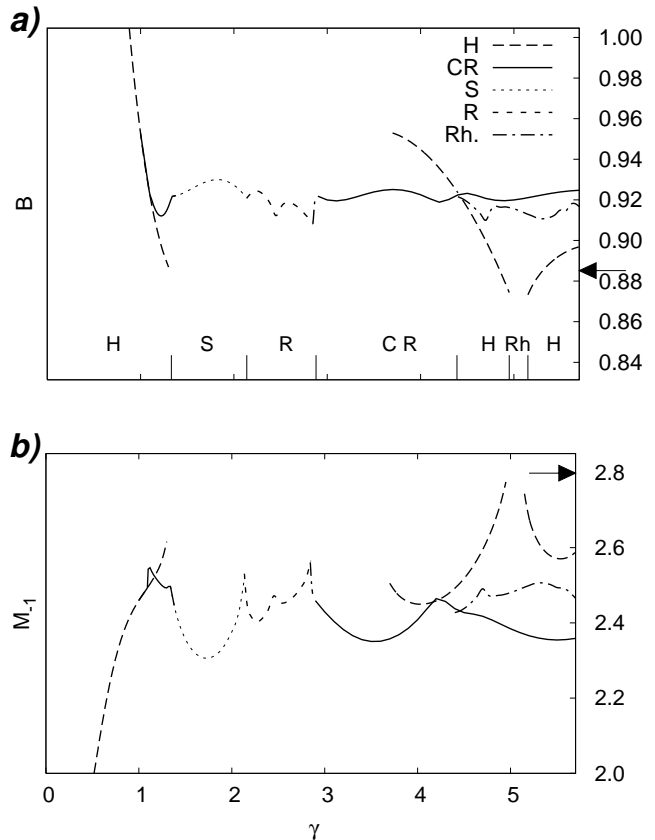


FIG. 2: a) Zero point vibrational term B for the different structures identified in Fig. 1, within their ranges of mechanical stability. The sequence of structures with the lowest vibrational energy is indicated at the bottom. The arrow indicates the value $(2/3)B^{(3D)} = 0.887$, where $B^{(3D)}$ is the vibrational energy of a BCC crystal in vacuum; b) Inverse moment M_{-1} of the DOS, which is proportional to the mean electronic fluctuation $\langle u^2 \rangle$ Eq.(12) for the same structures. The arrow indicates the value for a BCC in free space.

(D is the number of branches, corresponding to the dimensionality of the electron motion) as well its dimensionless moments:

$$M_n = \int d\omega \rho(\omega) \left(\frac{\omega}{\omega_P} \right)^n \quad (10)$$

with $\omega_P^2 = 3e^2/(mr_s^3)$ the usual 3D plasma frequency. With these definitions, the vibrational energy in Eq.(6) is seen to be directly proportional to the first moment of the DOS, with

$$B(\gamma) = \frac{D\sqrt{3}}{2} M_1(\gamma) \quad (11)$$

The usual 3D case in vacuum is recovered by restoring the out-of-plane oscillations in Eq. (4), and by setting $D = 3$ in Eq. (11). For example, for the BCC structure we find $M_1^{(3D)} = 0.511$, which yields the well known value $B^{(3D)} = 1.33$.^{25,31}

The analysis of the frequency spectrum shows that each given structure has a limited interval of mechanical stability: for certain geometries, the dynamical matrix acquires negative eigenvalues around some critical wavevector k_c , corresponding to purely imaginary collective frequencies which drive the crystal unstable (this phenomenon also exists in free space, where FCC and the simple cubic structure are known to be intrinsically unstable). For example, in the interval of γ under study, a structure with hexagonal symmetry is only stable for $\gamma < 1.32$, $3.5 < \gamma < 4.95$ and $5.05 < \gamma < 5.8$.

We have calculated the fluctuation term $B(\gamma)$ for the different symmetric structures (H, R, S, CR) identified in the previous section, within their respective intervals of mechanical stability, as well as for the rhombic phase at $2.84 < \gamma < 2.86$ and $\gamma > 4.31$, which is shown in Fig. 2.a. As for the Madelung energy, two essentially different regimes can be identified. For $\gamma \lesssim 1$, the electron motion is mostly determined by the Coulomb interactions within the layers (interlayer forces are negligible) and the collective modes of the pure 2D case are recovered. If normalized by an appropriate “two-dimensional plasma frequency” $\omega_{2D}^2 = e^2/mr_{s,2D}^3$, the first moment in the hexagonal phase tends to the constant value $M_{1,2D} = 0.814$.³² Going back to the present three-dimensional units, however, where the moments are normalized as in Eq.(10), the fluctuation term diverges at large separations as $B(\gamma) \simeq \pi^{1/4}3^{1/2}M_{1,2D}/2\gamma^{1/2}$. In the regime $\gamma \gtrsim 1$, on the other hand, the fluctuation term flattens around a value which roughly corresponds to 2/3 of the fluctuation in free space, indicated by the arrow in Fig. 2.a. This follows from the fact that only the oscillations along 2 of the 3 space directions are allowed, as we can see explicitly from Eq. (11).

The structural phase diagram resulting from the analysis of the total energy (6), including the vibrational term (11), and taking into account the ranges of mechanical stability of the different phases, is reported in Fig. 3. The first observation is that, apart from the disappearance of the CR phase from certain intervals, which is penalized by its higher vibrational energy than the H phase, the locus of the structural transitions does not change much with r_s . The sequence of phases identified in Fig. 1, based on the analysis of the Madelung energy, is recovered at extremely large values of r_s . On the other hand, the vibrational term affects the structural transitions already at $r_s \lesssim 1000$. This is due to the fact that, even though the electrostatic term A/r_s is still larger than the zero-point fluctuation energy $B/r_s^{3/2}$, the latter undergoes much larger relative variations among the different phases. Below $r_s \sim 100$, the phase diagram is entirely determined by the minimization of the vibrational energy (see Fig. 2.a). As was stated above, however, the overall shape of the phase diagram does not depend much on r_s , the transitions being essentially determined by the parameter γ . Let us also remark that the vibrational term is much less influenced than the Madelung term by the specific interlayer arrangements, whose effect (if any) is

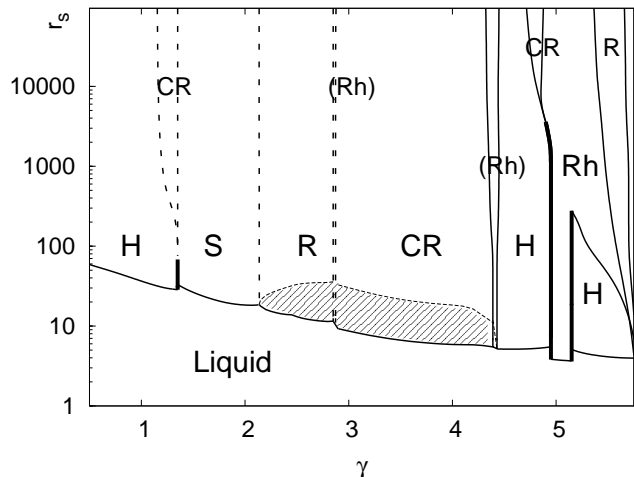


FIG. 3: Structural phase diagram of the Wigner crystal in a layered environment, based on the total energy (6), as a function of the anisotropy ratio γ and the bulk density parameter r_s . The labels are the same as in previous figures. The solid (dashed) lines are for structural transitions where the crystal parameters evolve discontinuously (continuously). The bold lines indicate mechanical instabilities, accompanied by a discontinuity of the crystal energy. The melting line is determined by solving Eq. (13). For the hatched region, see text.

to slightly modify the range of mechanical stability of each phase.

Another fundamental property of the system, which gives valuable informations on the collective vibrations of the particles, is the mean electronic fluctuation $\langle u^2 \rangle$. In the harmonic approximation, this quantity is proportional to the inverse moment of the DOS of the collective modes, defined in Eq. (10):

$$\langle u^2 \rangle = \frac{1}{N} \sum_{k,s} \frac{1}{2\omega_{k,s}} = \frac{DM_{-1}}{2\sqrt{3}} r_s^{3/2} \quad (12)$$

where again we keep track of the explicit dependence on the dimensionality D . As can be seen in Fig. 2.b, it increases as each phase approaches the boundaries of its stability range. This is because the mechanical instabilities are approached via a softening of a branch of collective modes, causing an increase of the DOS at low frequency and, through Eq. (10), of the inverse moment M_{-1} . A local increase also occurs at the points where the staggered interlayer ordering is lost (see e.g. the maximum at $\gamma = 2.46$ within the R phase in Fig. 2.b).

From analogous arguments, it follows from Eqs. (10) and (11) that the vibrational energy generally attains its minimum value close to mechanical instabilities. Within the present approximate framework, this can cause the total energy to jump discontinuously at the instability point when the next stable phase is attained, which corresponds to the bold lines in Fig. 3. For example, the hexagonal lattice becomes unstable at $\gamma > 1.33$ and, for

$r_s \lesssim 100$, the transition to the square phase is accompanied by a small jump in energy. Such discontinuities can in principle be avoided by allowing for Bravais lattices with more than one electron per unit cell (the resulting internal structure could then be assimilated to some local tendency to electron pairing^{33,34}). Note also that it is precisely close to mechanical instabilities, where $\langle u^2 \rangle$ is largest, that the neglected anharmonic corrections are expected to be most important. Their consequences on the structural phase diagram presented here deserve further theoretical study.

D. Melting of the crystallized state

In this section, we analyze the melting of the crystallized state by making use of the Lindemann criterion, according to which a transition to a liquid phase takes place when the spread $\langle u^2 \rangle$ attains some given fraction δ of the nearest-neighbor distance $a_{n.n.}$. We take $\delta = 0.28$ from Ref.³⁵, which is appropriate for the quantum melting of both 2D and 3D Wigner crystals. Solving the equation $\sqrt{\langle u^2 \rangle}/a_{n.n.} = \delta$ in terms of the density parameter $r_{s,2D}$ in the planes leads to:

$$r_{s,2D}^c = \frac{M_{-1}(\gamma)}{2\delta^2 \mathcal{C}^2(\gamma)} d^{1/2} \quad (13)$$

where $\mathcal{C} = a_{n.n.}/r_{s,2D}$ is an aspect ratio relating the nearest-neighbor distance to the density parameter in the planes, and the implicit condition $\gamma = \sqrt{\pi} r_{s,2D}^c/d$ holds. Note that for structures with rectangular symmetry, the Lindemann criterion must be modified to account for the existence of two nonequivalent near-neighbor distances. Here we use a simple generalization which consists in replacing $a_{n.n.}$ with the average of the two shortest near-neighbor distances, and which reduces to the ordinary criterion for the square and hexagonal structures. A check of the validity of such generalized Lindemann criterion will be given in Section II E, by direct comparison with independent theoretical results on bilayer systems.

The melting curve deduced from Eq. (13) for the different structures considered here is illustrated in Figs.3 and 4. The most important result is that the crystal melting can be pushed to higher densities by reducing the interlayer spacing, which can already be inferred by neglecting the weak γ -dependence of the coefficients \mathcal{C} and M_{-1} of Eq. (13) in the region $\gamma \gtrsim 1$. The main reason to this is that for $\gamma \gtrsim 1$ the electron spread is essentially governed by *three-dimensional* Coulomb interactions, as we can see from the explicit dependence of Eq. (12) on the bulk r_s , while the electron motion is *two-dimensional*, so that the appropriate nearest-neighbor distance for the Lindemann ratio is proportional to the *planar* density parameter $r_{s,2D} = (2/\sqrt{3d})r_s^{3/2}$.³⁶

In addition, for each given spacing d , the geometrical confinement leads to a further stabilization of the crystal through a reduction of the spread $\langle u^2 \rangle$ itself. This effect

is directly reflected in Fig. 2.b in a reduced value of M_{-1} as compared to the corresponding value in free space, and should not be confused with the trivial dimensional factor D , that was taken out explicitly from Eq. (12). It is due to the fact that, as soon as the cubic symmetry is lost, the restoring forces induced by the dipole-dipole interactions Eq. (5) are not equivalent in the three space directions, so that the electron fluctuation becomes anisotropic (the observed shrinking of the planar spread would occur at the expense of increasing the out-of-plane fluctuations, which are anyhow suppressed in the model). To give an example, taking an average value $M_{-1} \simeq 2.4$ and the aspect ratio $\mathcal{C} = \sqrt{\pi}$ for the square planar ordering yields a critical value $r_{s,2D}^c \simeq 4.9\sqrt{d}$. Comparable results (within few percent) are found for the other structures.

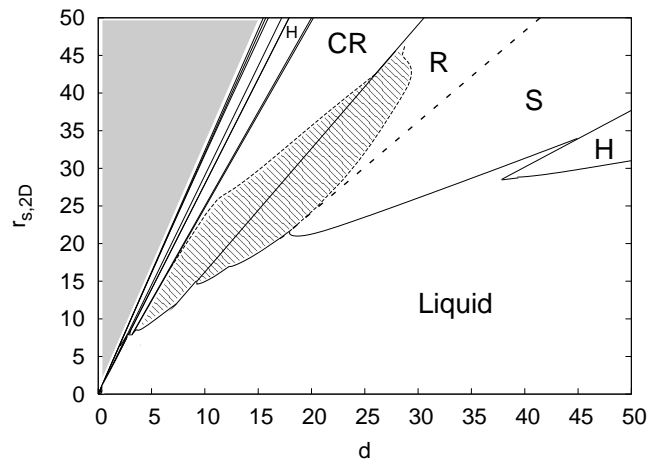


FIG. 4: Phase diagram of the Wigner crystal in a layered environment, as a function of the interlayer distance d (in units of the effective Bohr radius a_B^*). The discontinuity close to the three-phase critical point (S, H, liquid) is due to the different aspect ratios \mathcal{C} of the two competing structures. The hatched area is a region possibly characterized by an anisotropic liquid behavior (see text). The shaded area corresponds to $\gamma > 6$ and has not been studied.

In the opposite limit of large separations ($\gamma \ll 1$), where interlayer forces become negligible, we recover the usual critical value $r_{s,2D}^c \simeq 40$ for the 2D hexagonal Wigner crystal. Note that the actual critical value at finite γ always lies below this asymptotic estimate, confirming that the inclusion of interlayer interactions causes a stabilization of the crystal phase compared to the pure two-dimensional case, as was argued in the introduction.

A few comments on the limits of validity of the present model are in order. First, the enhancement of Wigner crystallization predicted by Eq. (13) cannot extend indefinitely: the melting line should eventually saturate at low separations when isotropic electron motion and three-dimensional screening are restored by interlayer tunneling processes.²³ On the other hand, as was stated in the introduction, replacing the host lattice of ions by an ef-

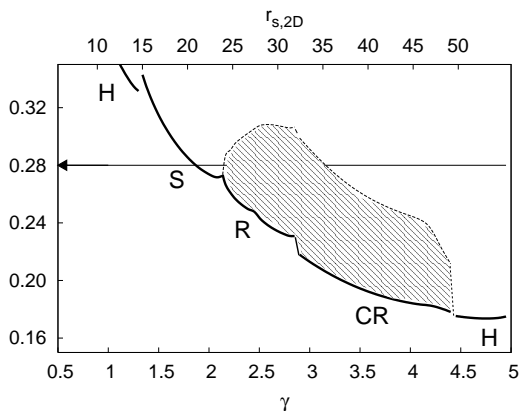


FIG. 5: Lindemann ratio $\sqrt{\langle u^2 \rangle}/a_{n.n.}$ as a function of γ ($r_{s,2D}$, upper abscissa) at a given interlayer spacing $d = 20$. The continuous line is the average Lindemann ratio, the dashed line represents the Lindemann ratio along the direction of the closest near-neighbor (see text). The horizontal line sets the critical value for melting. Upon increasing the electron density, the transition from the crystal to the liquid could occur through an intermediate anisotropic liquid phase (hatched region, see also Fig. 4).

fective jellium is allowed provided that the spread of the electron wavefunction is larger than the ion-ion distance a_0 . From eq. (12), the condition $\sqrt{\langle u^2 \rangle} \gtrsim a_0$ gives $r_s \gtrsim 4$ ($r_{s,2D} \gtrsim 6$) for a typical value of $a_0 = 3\text{\AA}$, assuming $\kappa = 1$ and $m^* = m$. Below this value, the discrete nature of the host lattice should be included, which can further stabilize the crystallized state, as pointed out in Refs.^{17,18,38}.

Before concluding this section, let us remark that, for anisotropic planar orderings such as the rectangular and the centered rectangular structure, two independent Lindemann ratios could in principle be defined (one for each nonequivalent near-neighbor direction) rather than the single average criterion used so far. It would then appear that the melting along the short bonds is much easier than along the long bonds, due to the closer overlap between the electron wavefunctions. This phenomenon is illustrated in Fig. 5, and could imply a tendency towards an anisotropic (or “striped”) liquid phase, which is generally not ruled out by the isotropic nature of the Coulomb repulsion (see also the hatched regions in Figs. 3 and 4).³⁷ The results reported in Fig. 5 also indicate a possible reentrant behavior, although no conclusive answer can be given at this level of approximation.

E. Symmetric electron bilayer

In this section we analyze a system composed of two coupled electronic layers, in order to check the validity of our approach by direct comparison with available Density Functional Theory²¹ and Quantum Monte Carlo based calculations^{22,23}. In the early work on classical bilayers,¹⁹

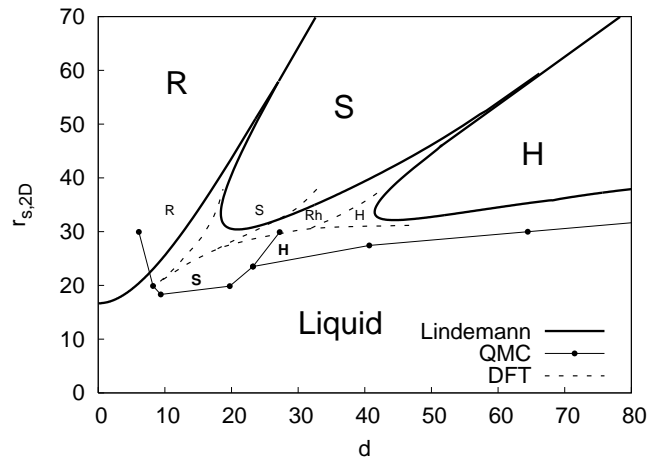


FIG. 6: Phase diagram for the symmetric electron bilayer, in terms of the two dimensional density parameter $r_{s,2D}$, as a function of the interlayer spacing d . The lengths are scaled to atomic units. H,S,R denote respectively the Hexagonal, Square, Rectangular phase. Note that the QMC simulation of Ref.²³ was restricted to study only two phases (H,S), while an additional rhombic phase (Rh) could be stabilized in the DFT calculations of Ref.²¹.

the analysis of the Madelung energy showed that several structural phase transitions occur as the distance d between the two planes is varied while keeping the electron density fixed. At short distances the planar ordering is rectangular, and collapses to the usual hexagonal phase in the formal limit $d \rightarrow 0$. This phase evolves continuously into a staggered square structure, when d is of the order of the interparticle spacing, which is clearly reminiscent of the BCC structure observed in 3D space (cf. the discussion in Section II B). Upon further increasing d , the lattice progressively deforms into a rhombic phase, to attain the hexagonal staggered phase expected in the limit of independent layers. Including the zero-point energy of the collective excitations as in Eq. (6) raises the energy of the rhombic phase, which therefore disappears from the phase diagram at sufficiently high density, leaving the other transitions essentially unchanged.

We have analyzed the quantum melting of the different Wigner crystal structures realized in such bilayer system by making use of the Lindeman criterion discussed in the preceding Section. We see from Fig. 6 that both the sequence of phases and the critical melting densities obtained within the present quadratic approximation are in satisfactory agreement with the more sophisticated numerical results of Refs.^{21,22,23} (the melting density is slightly underestimated as compared with QMC, but quite similar to the DFT result). It is interesting to see that the same trends observed in the preceding Section for the layered solids are already present in the single bilayer. In particular, reducing the interlayer separation leads to a sensible stabilization of the crystal compared

to the isolated layers. This is clear in Fig. 6, where the the melting line always lies below the critical value $r_{s,2D}^c \simeq 40$ of a purely 2D Wigner crystal. Note also that, contrary to Ref.²², we find that the enhancement of Wigner crystallization is slightly more pronounced in an infinite array of layers than in a single electron bilayer.

III. WIGNER CRYSTALLIZATION IN QUASI ONE-DIMENSIONAL SOLIDS

We now extend our analysis to the case of quasi one-dimensional solids, which we model as periodic arrays of conducting wires. Following the general arguments presented in the previous Section, the enhancement of Wigner crystallization in this case should be even more pronounced than in the two-dimensional case, because of the suppression of electronic motion in two transverse directions rather than one. The effect is even more dramatic if we consider that a quantum crystal with genuine long-range order cannot be realized in a pure one-dimensional system,³⁹ while it is stabilized if we account for the long-range Coulomb interactions between carriers on different wires.⁴⁴

We shall consider here a square array of wires for illustrative purposes, although the specific arrangements occurring in real solids (rectangular, rhombic) can be treated case by case. Assuming a simple ordering of period a within the wires and an interwire distance d , the most general elementary three-dimensional Bravais lattice compatible with the given geometrical constraint is described by the following basis vectors: $\hat{A}_1 = (0, 0, a)$, $\hat{A}_2 = (d, 0, b)$, $\hat{A}_3 = (0, d, c)$. The volume of the 3D unitary cell is $V_c = ad^2 \equiv 4\pi r_s^3/3$, the anisotropy ratio is now defined as $\gamma = a/d$ and the 1D density parameter is $r_{s,1D} = a/2$. As in the layered case, we take a compensating positive charge distributed uniformly in the bulk. The analysis presented in the preceding Section can be repeated here following the same steps: i) calculation of the structure with the lowest Madelung energy upon varying the anisotropy ratio; ii) calculation of the corresponding vibrational energies; iii) determination of the melting curve via the Lindemann criterion. The generalization is straightforward, and we only report here the main results.

The structural phase diagram (Fig. 7) is clearly less rich than in the layered case, because once the density and the interwire distance d are fixed, only the relative ordering between the electronic crystals on neighboring wires remains to be determined, corresponding to the pair of parameters b and c . In the limit $\gamma \rightarrow 0$, the interwire interactions vanish and the limit of isolated wires is recovered: the Madelung constant A diverges due to the isotropic distribution of the jellium, as explained previously (cf. footnote 43). In this limit the interwire ordering is staggered, with $b/a = c/a = 1/2$, corresponding to a body centered tetragonal (BCT) lattice in three-dimensional space. The BCT structure, everywhere compatible with

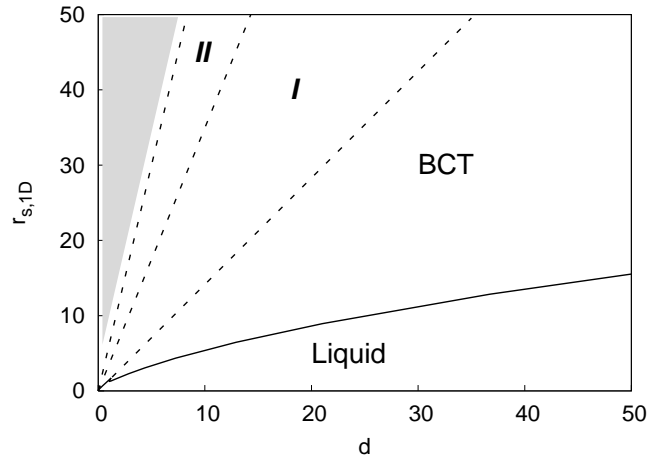


FIG. 7: Phase diagram for a three-dimensional Wigner crystal embedded in a square array of 1-dimensional wires, of side d . Lengths are scaled to effective atomic units. For the definition of the phases I and II, see text. The shaded region corresponds to $\gamma > 10$ (not studied).

a square array of wires, has the lowest Madelung energy in the whole range $0 < \gamma < 2.83$, with the two special values $\gamma^* = \sqrt{2}$ and $\gamma^* = 2$ corresponding respectively to a BCC and a FCC. For $\gamma > 2.83$ the minimum configuration becomes less symmetric, with $c/a \neq 1/2$ but the ratio b/a still locked to the value $1/2$ up to $\gamma = 6.99$. This phase is denoted (I) in Fig.7. Beyond $\gamma = 6.99$, a second structural transition occurs leading to a generic phase (II) with both $b/a \neq 1/2$ and $c/a \neq 1/2$. Other transitions can take place at larger values of γ , within the generic phase II. The sequence of phases does not change upon inclusion of the vibrational term.

By applying the Lindemann rule we obtain a parametric formula for the melting curve analogous to Eq. (13):

$$r_{s,1D}^c = \frac{1}{(128\pi)^{1/3}} \left[\frac{M_{-1}(\gamma)}{\delta^2} \right]^{2/3} d^{2/3} \quad (14)$$

with the implicit condition $\gamma = r_{s,1D}^c/2d$. The consequences of geometrical confinement evidenced in the layered case are recovered here. The electron spread along the wires is again governed by the three-dimensional plasma frequency [cf. Eq. (12)], due to the isotropic nature of the Coulomb interactions, while the nearest-neighbor distance here scales with $r_{s,1D} \equiv (2\pi/3)r_s^3/d^2$. Further stabilization of the crystallized state is achieved through a reduction of the electron spread along the wires, revealed by an inverse moment M_{-1} which is typically 50% lower than the value in vacuum. Its γ -dependence for $\gamma \gtrsim 1$ is quite flat (not shown), except in the vicinity of the transition at $\gamma = 2.85$, where it raises due to the mode softening discussed in Section II C. Replacing the average value $M_{-1} \simeq 2$ into Eq. (14) yields $r_{s,1D}^c \simeq 1.2d^{2/3}$, corresponding to an even stronger

enhancement of Wigner crystallization than in the layered case (see Table I). In the opposite anisotropic limit $\gamma \ll 1$, M_{-1} diverges as in the case of an isolated wire (cf. footnote 43), so that the Wigner crystal is never stabilized ($r_{s,1D}^c \rightarrow \infty$).

	γ	crystal melting	$d = 8a_B^*$	$d = 20a_B^*$
layers	$\sqrt{\pi}r_{s,2D}/d$	$r_{s,2D}^c \simeq 4.9 d^{1/2}$ $\gamma \gtrsim 1$ $\simeq 40$ $\gamma \ll 1$	14	21
wires	$2r_{s,1D}/d$	$r_{s,1D}^c \simeq 1.2 d^{2/3}$ $\gamma \gtrsim 1$ $\rightarrow \infty$ $\gamma \ll 1$	5	9

TABLE I: Definition of the anisotropy ratio γ , approximate melting lines obtained for quasi two-dimensional and quasi one-dimensional systems, and specific values obtained at two different interlayer (interwire) distances d , expressed in units of the effective Bohr radius a_B^* (right columns).

IV. CONCLUSIONS

We have investigated the Wigner crystallization of electrons in quasi low-dimensional compounds, where the carrier motion is effectively low-dimensional, while the Coulomb interactions are assumed long-ranged and isotropic. The system properties are found to depend crucially on the ratio γ of the mean interparticle spacing within the conducting units (layers or chains) to the separation d between units. While the behavior expected for

isolated units is recovered at large separations ($\gamma \ll 1$), an overall isotropic ordering of the charges is achieved for $\gamma \gtrsim 1$, when the interactions between different units become important. In this case, three-dimensional structures as close as possible to the ideal case of a BCC are formed, leading to a cascade of structural transitions which can be tuned by varying the particle density, or the distance d itself. In addition to this rich phase diagram, the presence of isotropic Coulomb interactions in such anisotropic compounds results in a strong stabilization of the charge ordered phases, possibly up to densities of practical interest, where the characteristic energy scales of the Wigner crystal can become comparable with other relevant scales in the solid. Although it is clear that the interplay with several other factors such as the periodic lattice potential,^{6,16,17,18,30,38} chemical impurities,⁴⁰ polarons^{15,27} or magnetic interactions^{14,41} should be considered for an accurate description of real materials, the long-range Coulomb interactions appear in light of the present study as a key ingredient to understand the charge ordering phenomena in quasi low-dimensional systems.

ACKNOWLEDGMENTS

We thank S. Ciuchi for critical and constructive discussions. G. R. thanks the kind hospitality of CNRS-LEPES Grenoble (France) and financial support by MIUR-Cofin 2004/2005 matching funds programs.

-
- ¹ E. P. Wigner, Phys. Rev. **46**, 1002 (1934), E. P. Wigner, Trans. Faraday. Soc. **34**, 678 (1938).
² R. S. Crandall, R. Williams, Phys. Lett. A **34** 404 (1971).
³ C. C. Grimes, G. Adams, Phys. Rev. Lett. **42**, 795 (1979).
⁴ E. Y. Andrei, *Two-Dimensional Electron Systems on Helium and other Cryogenic Substrates*, (Kluwer Academic Publ. 1997), pags. 245-279 and refs. therein.
⁵ J. Yoon, C. C. Li, D. Shahar, D. C. Tsui, M. Shayegan, Phys. Rev. Lett. **82**, 1744 (1999).
⁶ J. Hubbard, Phys. Rev. B **17**, 494 (1978).
⁷ F. Nad, P. Monceau, C. Carcel, and J. M. Fabre, Phys. Rev. B **62**, 1753 (2000); P. Monceau, F. Ya. Nad and S. Brazovskii, Phys. Rev. Lett. **86**, 4080 (2001).
⁸ D. S. Chow et al., Phys. Rev. Lett. **85**, 1698 (2000).
⁹ K. Hiraki and K. Kanoda, Phys. Rev. Lett. **80**, 4737 (1998); Y. Nakazawa et al., Phys. Rev. Lett. **88**, 076402 (2002).
¹⁰ P. Abbamonte et al., Nature **431**, 1081 (2004).
¹¹ A. Rusydi et al., cond-mat/0511524
¹² P. Horsch, M. Sofin, M. Mayr, and M. Jansen, Phys. Rev. Lett. **94**, 076403 (2005).
¹³ M. Dressel and N. Driehko, Chem. Rev. **104**, 5689 (2004).
¹⁴ H. C. Fu, J. C. Davis, D.-H. Lee, cond-mat/0403001 (unpublished).
¹⁵ G. Rastelli, S. Fratini, P. Quémerais, Eur. Phys. J. B **42**, 305 (2004).
¹⁶ D. Baeriswyl and S. Fratini, J. Phys IV France **131**, 247 (2005).
¹⁷ H. Falakshahi et al., Eur. Phys. J. B **39**, 93 (2004).
¹⁸ B. Valenzuela, S. Fratini and D. Baeriswyl, Phys. Rev. B **68**, 045112 (2003).
¹⁹ G. Goldoni, F. M. Peeters, Phys. Rev. B **53**, 4591 (1996).
²⁰ I. V. Schweigert, V. A. Schweigert, F. M. Peeters, Phys. Rev. Lett. **82**, 5293 (1999); I. V. Schweigert, V. A. Schweigert, F. M. Peeters, Phys. Rev. B **60**, 14665 (1999).
²¹ G. Goldoni, F. M. Peeters, Europhys. Lett. **37**, 293 (1997).
²² L. Świerkowski, D. Neilson and J. Szymański, Phys. Rev. Lett. **67**, 240 (1991).
²³ G. Senatore, F. Rapisarda and S. Conti, Int. J. Mod. Phys. B **13**, 5-6, 479 (1999).
²⁴ W. J. Carr, Phys. Rev. **122**, 1437 (1961).
²⁵ W. J. Carr, R. A. Coldwell-Horsfall, and A. E. Fein, Phys. Rev. **124**, 747 (1961).
²⁶ C. B. Clark, Phys. Rev. **109**, 1133 (1958).
²⁷ S. Fratini, P. Quémerais, Eur. Phys. J. B **14**, 99 (2000); *idem*, Eur. Phys. J. B **29**, 41 (2002); G. Rastelli, S. Ciuchi, Phys. Rev. B **71**, 184303 (2005).
²⁸ P. P. Ewald, Ann. Phys. **64**, 253 (1921).
²⁹ E. Ya. Sherman, Phys. Rev. B **52**, 1512 (1995).
³⁰ E. V. Tsiper and A. L. Efros, Phys. Rev. B **57**, 6949 (1998).
³¹ E. L. Pollock, J. P. Hansen, Phys. Rev. A **8**, 3110 (1973); R. Mochkovitch, J. P. Hansen, Phys. Letts. A **73**, 35 (1979).
³² L. Bonsall, A. A. Maradudin, Phys. Rev. B **15**, 1959 (2005).

- (1977); R. C. Gann, S. Chakravarty G. V. Chester, Phys. Rev. B **20**, 326 (1979).
- ³³ K. Mouloupoulos, N. W. Ashcroft, Phys. Rev. B **48**, 11646 (1993)
- ³⁴ Yu. G. Pashkevich and A. E. Filippov, Phys. Rev. B **63**, 113106 (2001)
- ³⁵ H. Nagara, Y. Nagata and T. Nakamura, Phys. Rev. A **36**, 1859 (1987).
- ³⁶ G. Rastelli, P. Quémerais and S. Fratini, J. Phys. IV France **131**, 277 (2005)
- ³⁷ A. A. Slutskin, V. V. Slavin, and H. A. Kovtun, Phys. Rev. B **61**, 14184 (2000)
- ³⁸ Y. Noda, M. Imada, Phys. Rev. Lett. **89**, 176803 (2002)
- ³⁹ H. J. Schulz, Phys. Rev. Lett. **71**, 1864 (1993)
- ⁴⁰ S. T. Chui and B. Tanatar, Phys. Rev. Lett. **74**, 458 (1995)
- ⁴¹ B. P. Stojkovic, Z. G. Yu, A. R. Bishop, A. H. Castro Neto and N. Grnbech-Jensen, Phys. Rev. Lett. **82**, 4679 (1999); V. M. Pereira, J. M. B. Lopes dos Santos, A. H. Castro Neto, cond-mat/0505741
- ⁴² The kinetic energy evaluated in the noninteracting limit is strongly reduced in lower dimensions, where there are less high momentum states available ($T = 1.11/r_s^2$, $0.5/r_{s,2D}^2$ and $0.11/r_{s,1D}^2$ in 3D, 2D and 1D respectively) while the Madelung energy in the opposite classical limit is less dependent on dimensionality [$E_{3D} = 0.896/r_s$ for the body centered cubic lattice, $E_{2D} = 1.11/r_{s,2D}$ for the hexagonal lattice]. Incidentally, the crystallization transition in both 3D ($r_s \simeq 100$) and 2D ($r_{s,2D} \simeq 40$) takes place at the same value of the ratio $E/T \simeq 81$.
- ⁴³ The usual value for the Madelung energy of the hexagonal lattice in two dimensions would be recovered at large interlayer separations by considering a layered compensating charge. This would not alter the sequence of crystal structures, since it would add a constant term to the energy depending only on the anisotropy ratio γ .
- ⁴⁴ This can be understood by observing that the logarithmic divergence of the mean spread $\langle u^2 \rangle \sim \int d\omega \omega^{-1}$ arising in 1D is washed out in the present case where the wires are embedded in a three-dimensional environment and momentum integrations run over the 3D Brillouin zone.